The role of micro cavitation on EHL: a study using a multiscale mass conserving approach

Leiming Gao[1], Gregory de Boer[2] and Rob Hewson[3]

[1,3] *Department of Aeronautics, Imperial College London, London, SW7 2AZ, UK*
[2]*School of Mechanical Engineering, University of Leeds, Leeds, LS2 9JT, UK*

[1] Corresponding author, Email: leiming.gao@gmail.com; Tel: +44 (0)20 7594 1976

KEYWORDS

Cavitation; Multiscale; Textured Surface; Elastohydrodynamic Lubrication (EHL).

ABSTRACT

The role of micro cavitation in Elastohydrodynamic Lubrication is numerically investigated using a multiscale approach whereby both the small scale topographical features and the micro-cavitation of the lubricant due to the features are resolved. Micro-cavitation and the fluid's shear-thinning property are modelled at the small scale of topological feature. The effects of topographical features on the film thickness of the line contact bearings and friction coefficient are presented with a focus on the role of micro-cavitation. This highlights how a mass conserving small scale model can be used to model both micro-cavitation and cavitation occurring at the bearing scale, and how topological features can be designed to reduce friction while maintaining bearing load.

1   **1 INTRODUCTION**
2
3   In this paper the role of cavitation in an Elastodhydrodynamic Lubrication (EHL) converging-

4   diverging line contact is investigated. The bearing surfaces are a smooth moving roller surface

5   relative to a stationary, textured flat surface. Topographical changes to a lubricated surface of

6   industrial components have been experimentally and numerically shown to improve their

7   tribological performance in three main aspects, the load carrying capacity, the friction

8   coefficient and the lubricant fluid film [1, 2]. Such applications include piston rings [3, 4],

9   mechanical seals [5, 6], journal bearings [7, 8], pad bearings [9-12] and roller bearings in line

10 contacts [13-17] and point contacts [18, 19].

11   A number of numerical approaches have been proposed to represent lubrication of surfaces

12 with topographical features [7, 17, 18, 20, 21]. One of the challenges of numerically describing

13 these problems is the order of magnitudes difference in the size of bearing surface topography

14 and the bearing itself. This has led to a number of multiscale methodologies to analyse the

15 problem and overcome the limitation in terms of computing costs [22-26]. Among the

16 multiscale models, many of them employ an adapted Reynolds equation based on Patir and

17 Cheng's average flow model [27] to solve the large scale fluid pressure, and the Stokes or

18 Navier-Stokes equations to solve the small scale fluid flow [22, 24, 26]. Recently, the

19 homogeneous multiscale approach has been developed, in which the large scale fluid flow was

20 governed by a homogeneous pressure-gradient function whose coefficient was obtained from

21 the small scale simulations. These include the work of Nyemeck et al. [25] on the

22 hydrodynamic lubrication with rigid bearing surfaces of seals, and the authors' work [11, 12] on

23 the EHL simulation of micro-textured pad bearings.

24   The role of micro-cavitation on lubrication has been studied by a number of investigators

25 arising from experimental observation of cavitation occurring in the vicinity of surface

26 roughness [20, 28]. The role of cavitation raises further questions regarding the validity of

27 using a form of the lubrication equation, where cavitation effects may not be uniform across

28 the film thickness due to the underlying topography; this cannot be captured by the lubrication

29 approximation where a constant pressure is assumed across the film thickness. Olver et al. [29]

30 proposed an 'inlet suction' effect due to fluid flow driven by cavitation pressures located in the

inlet region of the pad bearing surface. Ausas et al. [30] and Qiu and Khonsari et al. [31] studied micro-cavitation in textured bearing lubrication using a mass conserving model and compared different boundary conditions of cavitation; the half-Sommerfield condition, Swift-Steiber (Reynolds) condition and the Floberg–Jakobsson–Olsson (JFO) condition. It was found that the Reynolds condition largely underestimated the cavitation area and predicted a higher load-carrying capacity than the JFO results. Other studies of micro-cavitation have used Navier-Stokes based Computational Fluid Dynamics (CFD) simulations to solve the fluid flow, for example, Shi and Ni [32], Wahl et al. [33] and Meng and Yang [34]. However, these studies of micro-cavitation were all modelled at a single scale, where the topographical features were described over the entire lubrication domain. The number of simulated micro dimples or grooves in these studies was limited to up to 10 due to the very fine mesh required to resolve the small scale features and cavitation. In real engineering applications the number of micro dimples (and roughness) could be much larger on a real textured bearing's surface, and a multiscale method is especially relevant to solve such problem.

In this paper the heterogenous multiscale method (HMM) [35] is applied to EHL as derived by the authors [11, 12, 36] and extended to include cavitation effects, via the application of a mass-conserving approach at both small and large scales. This enables the model to capture cavitation at both scales. The pressure gradient-mass flow rate relationship is obtained from a homogenised local scale solution. This relationship is subsequently used at the global scale as a governing equation of fluid flow, and solved along with the conservation of mass. In this work cavitation is considered at the local scale via a predefined threshold cavitation pressure. The effects of the micro-texture's geometrical parameters on the bearings' lubrication film thickness and friction coefficient are presented. The piezo-viscous and shear-thinning effects are discussed and the importance of the role of micro cavitation at the small scale is highlighted.

2 NUMERICAL METHODOLOGY

2.1   Geometry and Materials

1   In this study, the global geometry of the lubrication model is a two-dimensional cylindrical

2   line contact. The smooth cylinder rotates relative to a textured stationary surface, as shown in

3   Fig. 1. The material of the plane is PTFE with an elastic modulus (E) of 0.5 GPa and Poisson's

4   ratio (v) of 0.4. The cylinder is assumed to be rigid compared to the soft PTFE bearing surface.

5   The radius of the cylinder (r) is 25 mm and the rotation speed (ω) is 80 rad/s, and equivalent to

6   a sliding speed (U_0) of 2 m/s. The micro-pocket length (L) ranges from 20 μm and 100 μm and

7   the depth (d) from 0 μm and 30 μm. The geometrical and material parameters are listed in

8   Table 1.

9

10   **2.2   Large Scale Simulation**

11   The large scale simulation describes the fluid-structure interaction in the global lubrication

12   domain, where the fluid pressure is solved simultaneously with the elastic deformation of the

13   bearing surfaces. The difference between the current study and classical EHL analysis is that

14   the governing equation for the hydrodynamic pressure is a homogenised equation from the

15   small scale simulations, rather than the Reynolds equation, expressed as

$$\frac{d\hat{p}}{dx} = f(g, \hat{p}, \dot{m}) \tag{1}$$

16   together with the mass conservation equation

$$\frac{d\dot{m}}{dx} = 0 \tag{2}$$

17   The pressure gradient ($\frac{d\hat{p}}{dx}$) is a homogenised function of the pressure ($\hat{p}$), mass flow rate ($\dot{m}$)

18   and film gap (g), interpolated from a series of small scale solutions. The large scale boundary

19   conditions used to solve Eqs. (1) and (2) are that the pressure at the bearing inlet and outlet

20   boundaries is equal to zero:

$$\hat{p}_{in} = \hat{p}_{out} = 0 \tag{3}$$

21   The line contact bearing load is balanced by an integral of the average small scale pressure

22   (i.e., load per unit length p^*), along the line contact domain. The average small scale pressure

23   (p^*) was defined in Eq. (17) in the Section 2.3.1 'Small Scale Simulations'.

$$w = \int_{xin}^{xout} p^* \, dx \tag{4}$$

The geometry equation is expressed as a sum of the rigid displacement (e, an unknown constant determined by load w), rigid gap geometry and the surface deformation (δ):

$$h = e + \frac{x^2}{2r} + \delta \tag{5}$$

$$\delta = \boldsymbol{K} \times p^* \tag{6}$$

where the displacement influence coefficient matrix $\boldsymbol{K}$ was obtained using the Green's function [37] for linear elastic contact model.

2.3   Small Scale Simulations

The small scale problem is described by the flow equations and those governing the elastic deformation of the small scale features. The coupling is facilitated through the application of the Arbitrary Largrangian Eularian (ALE) method to describe the fluid domain as the solid domain deforms and the inclusion of non-Newtonian, piezo-viscous and cavitation effects are included.

2.3.1 Solid Structure Model

The small scale solid domain is described by a plain strain model with the separation of the displacement influence coefficient matrix $\boldsymbol{K}$ into local (diagonal, $\boldsymbol{K}_1$) and global (off-diagonal, $\boldsymbol{K}_2$) terms [12]. The film gap (g) at the small scale is described by the sum of undeformed gap and the non-local deformation ($\boldsymbol{K}_2 \times p$), not including the local deformation ($\boldsymbol{K}_1 \times p$).

$$g = e + \frac{x^2}{2r} + \boldsymbol{K}_2 \times p \tag{7}$$

The local terms are represented as part of the local fluid-structure interaction simulation, and the global terms are applied as they would be in a conventional EHL simulation. An equivalent height of the solid domain is introduced in order to ensure that the local deformation in the small scale simulations is the same as the column deformation obtained from the diagonal matrix. For further details of the structure model the reader is referred to references [12].

2.3.2 Laminar Flow Model

The steady-state, isothermal and laminar flow is governed by the compressible Navier-Stokes equations:

$$\rho(\mathbf{u} \cdot \nabla)\mathbf{u} = \nabla \cdot \left[-p\mathbf{I} + \eta\left(\nabla\mathbf{u} + (\nabla\mathbf{u})^{\mathrm{T}}\right) - 2\eta/3(\nabla \cdot \mathbf{u})\mathbf{I}\right] \tag{8}$$

$$\nabla \cdot (\rho\mathbf{u}) = 0 \tag{9}$$

where, $\mathbf{u}$ is the fluid velocity vector and $\mathbf{I}$ the unit tensor. ρ is the generalized fluid density which is a function of pressure based on Dowson-Higginson formula [38],

$$\rho = \theta \cdot \rho_0 \frac{c_1 + c_2 \cdot p}{c_1 + p} \tag{10}$$

where, c_1 and c_2 are the density-pressure coefficients, ρ_0 is the density at ambient pressure, θ is the density fraction of liquid in the liquid and gas mixture and is defined in the cavitation model in Section 2.3.2. Piezo-viscous effects are described by an exponential relationship [39], the viscosity of liquid and gas mixture (η) is expressed as:

$$\eta = \theta \cdot \eta^* \exp(\alpha \cdot p) \tag{11}$$

with the pressure-viscosity coefficient α. Considering the fluid shear-thinning property, the generalized viscosity η^* is defined using a Carreau viscosity model [40] below.

$$\eta^* = \eta_\infty + (\eta_0 - \eta_\infty)[1 + (\eta_0\,\dot{\gamma}/G_{cr})^2]^{\frac{m-1}{2}} \tag{12}$$

where, $\dot{\gamma}$ is shear rate. η_0 and η_∞ represent the dynamic viscosity at zero shear rate and infinite shear rate, respectively. G_{cr} is critical stress at ambient pressure. The piezo-viscous effect described in Eq. (11) and the shear-thinning property defined in Eq. (12) are illustrated in Fig. 2.

The boundary conditions are shown in Fig. 1b. The lower boundary CD (Fig. 1b) is a sliding wall. The upper fluid-structure interface is a no slip boundary. In heterogenous multiscale method, periodic boundary conditions are required on the AD and BC boundary in terms of fluid velocity and pressure. Due to small scale deformation the two boundary geometries are not exactly the same, therefore, the boundary BC was scaled to the same length of boundary AD in the reference coordinates (undeformed gap) [12]. Near-periodic velocity boundary conditions are derived from the mass conservation at the two boundaries, scaled by the local strain ε:

$$\rho_1\boldsymbol{u}_1(1 + \varepsilon_1) = \rho_2\boldsymbol{u}_2(1 + \varepsilon_2) \tag{13}$$

1 and a pressure jump (Δp) is applied onto the scaled boundaries:

$$p_2 = p_1 + \Delta p \tag{14}$$

2 where, subscript 1 and 2 represent the scaled boundary AD and BC in Fig. 1b respectively. Since

3 the moving wall (lower surface) was fully constrained, i.e. there was no deformation allowed

4 and the strain was zero, the velocities at both sides of the fluid domain on the moving wall

5 surface were the same. Thus the nearly periodic conditions described in Eq. (**Error! Reference**

6 **source not found.**) are the same as periodic conditions at the moving surface and it satisfies

7 the no-slip boundary conditions.

8 The homogenised pressure gradient ($\frac{d\hat{p}}{dx}$) across a unit cell and a pressure jump across the small

9 scale cell is described by:

$$\frac{d\hat{p}}{dx} = \frac{\Delta p}{L} \tag{15}$$

10 The mass flow rate ($\dot{m}$) is calculated as:

$$\dot{m} = \int_0^{g+K_1 \times p} \rho u \, dy \tag{16}$$

11 An average pressure ($p*$) is defined to represent the cell pressure in large scale solutions:

$$p^* = \int_0^L p \, dx / L \tag{17}$$

12 The shear stress τ (shear force per unit length) is calculated as:

$$\tau = \int_0^L \eta^* \frac{du}{dy} \, dx / L \tag{18}$$

13

14 **2.3.3 Cavitation Model**

15 The lubricant is assumed to be a homogeneous mixture of liquid and gas. When the fluid

16 pressure drops below the saturation pressure cavitation occurs and some gas dissolved in fluid

17 will come out of solution. The density fraction of liquid (θ) is defined as a continuous function

18 of pressure using the hyperbolic tangent function:

$$\theta = 0.5 \times (1 + \tanh \frac{p - p_c}{k}) \tag{19}$$

1   The constants k are used to determine the steep gradient of the density fraction with respect

2   to a threshold cavitation pressure $p_c = -30$ KPa. The variation of θ against pressure is shown

3   in Fig. 3. The relationship described here is similar to the polynomial based approach used by

4   Almqvist and Larsson [41], to describe the density of lubricant with the fluid pressure. The

5   parameters of fluid properties are given in Table 2, and are based on mineral oil of the type

6   typically used as bearing lubricant [42, 43].

7

8

9   **2.4   Homogenisation of the pressure gradient equation**

10   The homogenised relationship between the pressure gradient and mass flow rate links the

11   small scale and large scale simulations. This relationship is obtained via interpolation. In order

12   to obtain an accurate representation of the small scale model, a range of small scale

13   simulations were undertaken for a range of gaps (g), homogenised pressure gradients ($\frac{\Delta p}{L}$) and

14   cell inlet pressures (p_1). A linear interpolation function was adopted, based on a Delaunay

15   triangulation of the data using Quickhull algorithm as implemented in Matlab [44]. To obtain

16   effective data samples for the interpolation, the range of input parameters are selected as

17   shown in Table 3 with total number of 3000 sample points, based on the corresponding results

18   of the smooth surface case of Reynolds equation.

19

20   Small scale solutions were obtained using the finite element method as implemented in

21   COMSOL Multiphysics. The variables are transformed to the non-dimensional forms for

22   convenience of numerical computing, for the global scale,

$$X, Y = x, y / R_{Hz}, G = \frac{g}{L}, \hat{P} = \frac{\hat{p}L}{\eta_0 U_0}, \frac{d\hat{P}}{dX} = \frac{d\hat{p}}{dx} \cdot \frac{L^2}{\eta_0 U_0}, \dot{M} = \frac{\dot{m}}{\rho_0 U_0 L} \tag{20}$$

23   and for the small scale,

$$P_1 = \frac{p_1 L}{\eta_0 U_0} \tag{21}$$

24

25   where R_{Hz} is the Hertzian contact radius,

$$R_{Hz} = \sqrt{\frac{8wr}{\pi E'}} \tag{22}$$

Subsequently, the pressure gradient equation is obtained via linear interpolation,

$$\frac{d\hat{P}}{dX}(i) = f\left[P_1, G, \dot{M}, \frac{d\hat{P}}{dX}, \hat{P}(i), G(i), \dot{M}\right], i = 1, \dots, n \tag{23}$$

where the first four parameters on the right-hand side $(P_1, G, \dot{M}, \frac{d\hat{P}}{dX})$ were known and obtained from small scale analysis. n denotes the mesh points at the large scale domain. The non-dimensional mass conservation equation is expressed as,

$$\frac{d\dot{M}}{dX}(i) = 0, , i = 1, \dots, n \tag{24}$$

3 Results

A non-dimensional large scale domain of $X = [-4, 2]$ and a fixed load of 2500 N was considered in this study. Large scale mesh independence tests were undertaken from 60 to 960 points in the large scale domain. For the Newtonian case with a smooth surface, the relative errors in the large-scale pressure and mass flow rate using different mesh are presented in Fig.4 (a), and the large-scale pressure distributions are compared in Fig.4 (b) and (c). The presence of smooth surface solutions allowed comparison with the solution obtained using Reynolds equation. In current study the number of mesh nodes n was set at 120, at which level the relative errors were approximately 7% and 5% in pressure and mass flow rate respectively. Four fluid viscosity models were investigated, i.e. (i) Newtonian, (ii) Newtonian and piezo-viscous, (iii) shear-thinning, and (iv) both piezo-viscous and shear-thinning. In each model, a range of cell lengths (L = 20, 50 and 100 μm) and depths (d = 0 ∼ 30 μm, increased by 5 μm) were considered. The friction coefficient and minimum film thickness are presented in Fig. 5. Typical results showing how cavitation is captured at the large scale is shown in Fig. 6 (a) and (b) for the case of L = 100 μm and d = 30 μm, where the large scale homogenised pressure and viscosity are presented from the small scale simulations, and the elastic deformation of the bearing surface also presented. The development of cavitation at small scale is demonstrated

9

1   in Fig. 6 (c) and (d), in the large scale outlet zone in the region of X = [0.8, 1.8]. The role of

2   shear thinning fluid properties is demonstrated in Fig. 7, where the homogenised viscosity is

3   clearly observed to decrease in the main loading domain at the large scale. The combination of

4   both piezo-viscosity and shear-thinning effect on the pressure, viscosity and film thickness is

5   shown in Fig. 8.

6

7   **4 Discussion**

8

9   **4.1. Fluid Rheology**

10   It can clearly been seen from these results that through the careful selection of small scale

11   depth and length, that the friction coefficient can be reduced. The friction coefficient is

12   presented as a function of the depth to length ratio (d/L) in Fig. 5, these results imply that

13   there is an optimal cell depth and length to achieve minimum friction. For example, in the

14   Newtonian cases, for the cell length L = 50 μm the minimum friction coefficient was observed

15   with the cell depth d = 10 μm and the reduction in the friction coefficient is 42% compared to

16   the smooth surface; for the cell length L= 100 μm the friction coefficient is reduced by 52%

17   when the cell depth d is 15 μm. This is similar to the results previously obtained by Gao and

18   Hewson [36] who obtained a similar trend for a slider bearing with the same small scale

19   surface features. In these cases there was a monotonic decrease in the friction with increasing

20   small scale length to depth ratio (d/L). What is interesting to note is that contrary to the

21   previous case there is a clear minimum friction coefficient predicted for a cell depth to length

22   ratio of around 0.15 for the cases of $L \geq 50$ μm. In the previous case it was observed that the

23   friction coefficient decreased then plateaued out to a near constant friction coefficient with

24   increasing cell depth.

25   While the different fluid rheologies considered all exhibit similar characteristics it should be

26   noted that the reduction in friction is most pronounced for the shear thinning fluid

27   characteristics, where there is a 3 fold decrease in the friction coefficient for the largest cell

28   geometry L = 100 μm. The effect of piezo-viscous is not significant for a low pressure values

29   encountered in the current study. The variations in the pressure, viscosity and film thickness

1   are less than 10% by comparing the results with or without piezo-viscous effect considered, as

2   shown in Figs. 7 and 8.

3   The minimum film thickness decreases with increasing cell depth as shown in Fig. 5, and this

4   has been reported in other EHL studies of textured surface [18, 20, 45]. Examining the

5   minimum film thickness shows how there is a clear compromise to be made between reducing

6   friction and maintaining a reasonable fluid film, as the effect of topography is to reduce the

7   minimum film thickness, with the greatest effect observed for the shear thinning fluid model.

8   The reasonable fluid film should have a minimum value which is double or triple the surface

9   roughness, i.e. the lambda ratio is 2 or 3, which means the bearing could operate in the mixed

10   or full film lubrication regime.

11

12   **4.2. Micro-Cavitation**

13   Cavitation was included in the small scale geometry, permitting the modelling of the

14   converging-diverging geometry to be modelled without a specific large scale treatment of

15   cavitation. The pressure distributed over the whole lubrication domain was governed by the

16   homogenised pressure equation. This is different from classical EHL models, where the

17   Reynolds boundary condition (pressure is positive everywhere) is commonly applied in the

18   diverging geometry. Since the small scale pocket itself is a divergent-convergent geometry, the

19   local pressure usually decreases at the inlet divergent edge, and then increase at the outlet

20   convergent edge. When there is limited cavitation in the small scale the local pressure

21   distributed is nearly anti-symmetrically (as shown by the top curve in Fig. 6 (c), at location X =

22   0.8). When cavitation extended towards outlet zone, i.e. X increases, the pressure field

23   diverges from this. The cavitation region can be observed in Fig. 6 (d) where the region of low

24   density fraction indicates a larger cavitated zone as X increases. As the region of cavitation

25   increases further the local pressure became nearly constant of -30 KPa (as shown by the

26   bottom curve in Fig. 6 (c), at location X = 1.8).

27   What is interesting is that there is a rise in viscosity in the diverging region before cavitation

28   occurs as shown in Fig. 7. This can also be observed when piezo-viscosity is also added to the

29   model as is shown in Fig. 8.

1

5 CONCLUSION

A heterogeneous multiscale model has been developed for the fluid-structure interaction in cylindrical line contact EHL with the bearing surface topography addressed. Fluid cavitation is explicitly modelled at the small scale via a continuous function of the fluid density and viscosity with pressure. The small scale cavitation effects are passed to the large scale model via the homogenised small scale relationship without further large scale treatment of cavitation. Such an approach also allows a range of rheological models to also be considered. The shear-thinning effects have been found to have significant effect on the bearing performance as well as the optimum small scale features required for optimum performance.

NOMENCLATURE

d	Cell depth [m]
E	Young's modulus [Pa]
E'	Equivalent Young's modulus [Pa]
e	Rigid displacement [m]
h	Large scale film thickness [m]
g	locally undeformed gap [m]
K	Displacement influence coefficient matrix [m^3/N]
L	Cell length [m]
n	Number of large-scale mesh grid
p	Pressure [Pa]
p_c	Threshold cavitation pressure [Pa]
$\dot{m}$	Mass flow rate per unit length [kg/m/s]
r	Radius of cylinder [m]
t'	Equivalent small-scale cell height [m]
U_0	Sliding speed of the roller [m/s]

$\boldsymbol{u}$	Fluid velocity vector [m/s]
w	One-dimensional load per unit length [N/m]
x	Coordinate in direction of fluid flow [m]
X	Dimensionless coordinate of x
α	Pressure-viscosity coefficient
$\dot{\gamma}$	Shear rate [1/s]
δ	Elastic deformation [m]
ε	Strain
η_0	Viscosity at zero shear rate [Pa s]
η_∞	Viscosity at infinite shear rate [Pa s]
η	Generalized viscosity in Carreau model [Pa s]
θ	Density fraction in cavitation model
μ	Friction coefficient
σ	Normal stress [Pa]
τ	Shear stress [Pa]
ν	Poission's ratio
ρ_0	Ambient fluid density [kg/m^3]
ρ	Generalized fluid density [kg/m^3]
ω	Rotation velocity of cylinder [rad/s]

REFERENCES

[1] Segu DZ, Choi SG, Choi JH, Kim SS. The Effect of Multi-Scale Laser Textured Surface on Lubrication Regime. Appl Surf Sci. 2013;270:58-63.

[2] Braun D, Greiner C, Schneider J, Gumbsch P. Efficiency of laser surface texturing in the reduction of friction under mixed lubrication. Tribol Int. 2014;77:142-47.

[3] Ryk G, Etsion I. Testing piston rings with partial laser surface texturing for friction reduction. Wear. 2006;261:792-96.

[4] Tomanik E. Modelling the hydrodynamic support of cylinder bore and piston rings with laser textured surfaces. Tribol Int. 2013;59:90-96.

[5] Etsion I, Kligerman Y, Halperin G. Analytical and Experimental Investigation of Laser-Textured Mechanical Seal Faces. Tribol Trans. 1999;42:511-16.

[6] Brunetiere N, Tournerie B. Numerical analysis of a surface-textured mechanical seal operating in mixed lubrication regime. Tribol Int. 2012;49:80-89.

[7] Dobrica MB, Fillon M, Maspeyrot P. Mixed elastohydrodynamic lubrication in a partial journal bearing-comparison between deterministic and Stochastic models. ASME J Tribol. 2006;128:778-88.

[8] Rao TVVLN, Rani AMA, Nagarajan T, Hashim FM. Analysis of slider and journal bearing using partially textured slip surface. Tribol Int. 2012;56:121-28.

[9] Dobrica MB, Fillon M, Pascovici MD, Cicone T. Optimizing surface texture for hydrodynamic lubricated contacts using a mass-conserving numerical approach. Proc Inst Mech Eng, Part J: J Eng Tribol. 2010;224:737-50.

[10] Sharma SC, Yadav SK. Performance analysis of a fully textured hybrid circular thrust pad bearing system operating with non-Newtonian lubricant. Tribol Int. 2014;77:50-64.

[11] de Boer GN, Hewson RW, Thompson HM, Gao L, Toropov VV. Two-scale EHL: 3D Topography in Slider Bearings. Tribol Int. 2014;79:111-25.

[12] Gao LM, Hewson R. A Multiscale Framework for EHL and Micro-EHL. Tribol Trans. 2012;55:713-22.

[13] Hao LC, Meng YG, Chen C. Experimental investigation on effects of surface texturing on lubrication of initial line contacts. Lubr Sci. 2014;26:363-73.

[14] Janakiraman S, Klit P, Jensen NS, Gronbaek J. Observations on the effects of grooved surfaces on the interfacial torque in highly loaded rolling and sliding tests. Tribol Int. 2015;81:179-89.

[15] Marian VG, Predescu A, Pascovici MD. Theoretical analysis of an infinitely wide rigid cylinder rotating over a grooved surface in hydrodynamic conditions. Proc Inst Mech Eng, Part J: J Eng Tribol. 2010;224:757-63.

[16] Vrbka M, Krupka I, Samanek O, Svoboda P, Vaverka M, Hartl M. Effect of surface texturing on lubrication film formation and rolling contact fatigue within mixed lubricated non-conformal contacts. Meccanica. 2011;46:491-98.

[17] Wang XL, Liu W, Zhou F, Zhu D. Preliminary Investigation of the Effect of Dimple Size on Friction in Line Contacts. Tribol Int. 2009;42:1118-23.

[18] Zhu D, Nanbu T, Ren N, Yasuda Y, Wang QJ. Model-Based Virtual Surface Texturing for Concentrated Conformal-Contact Lubrication. Proc Inst Mech Eng, Part J: J Eng Tribol. 2010;224:685-96.

[19] Kaneta M, Guo F, Wang J, Krupka I, Hartl M. Formation of Micro-Grooves Under Impact Loading in Elliptical Contacts with Surface Ridges. Tribol Int. 2013;65:336-45.

[20] Mourier L, Mazuyer D, Ninove FP, Lubrecht AA. Lubrication Mechanisms with Laser-Surface-Textured Surfaces in Elastohydrodynamic Regime. Proc Inst Mech Eng, Part J: J Eng Tribol. 2010;224:697-711.

[21] Minet C, Brunetiere N, Tournerie B. A Deterministic Mixed Lubrication Model for Mechanical Seals. ASME J Tribol. 2011;133.

[22] de Kraker A, Ostayen R, Beek A, Rixen D. A Multiscale Method Modelling Surface Texture Effects. ASME J Tribol. 2007;129:221-30.

[23] Demirci I, Mezghani S, Yousfi M, El Mansori M. Multiscale Analysis of the Roughness Effect on Lubricated Rough Contact. ASME J Tribol. 2014;136.

[24] Jai M, Bou-Said B. A Comparison of Homogenization and Averaging Techniques for the Treatment of Roughness in Slip-Flow-Modified Reynolds Equation. ASME J Tribol. 2002;124:327-35.

[25] Nyemeck AP, Brunetiere N, Tournerie B. A Multiscale Approach to the Mixed Lubrication Regime: Application to Mechanical Seals. Tribol Lett. 2012;47:417-29.

[26] Sahlin F, Larsson R, Almqvist A, Lugt P, Marklund P. A Mixed Lubrication Model Incorporating Measured Surface Topography. Part 1: Theory of Flow Factors. Proc Inst Mech Eng, Part J: J Eng Tribol. 2010;224:335-51.

[27] Patir N, Cheng HS. Average Flow Model for Determining Effects of 3-Dimensional Roughness on Partial Hydrodynamic Lubrication. ASME J Lubric Tech. 1978;100:12-17.

[28] Shen C, Khonsari MM. On the Magnitude of Cavitation Pressure of Steady-State Lubrication. Tribol Lett. 2013;51:153-60.

[29] Olver AV, T Fowell M, Spikes HA, Pegg IG. 'Inlet Suction', A Load Support Mechanism in Non-Convergent, Pocketed, Hydrodynamic Bearings. Proc Inst Mech Eng, Part J: J Eng Tribol. 2006;220:105-08.

[30] Ausas R, Ragot P, Leiva J, Jai M, Bayada G, Buscaglia GC. The Impact of the Cavitation Model in The Analysis of Microtextured Lubricated Journal Bearings. ASME J Tribol. 2007;129:868-75.

[31] Qiu Y, Khonsari MM. On the Prediction of Cavitation in Dimples Using a Mass-Conservative Algorithm. ASME J Tribol. 2009;131:041702.

[32] Shi X, Ni T. Effects of Groove Textures on Fully Lubricated Sliding with Cavitation. Tribol Int. 2011;44:2022-28.

[33] Wahl R, Schneider J, Gumbsch P. In Situ Observation of Cavitation in Crossed Microchannels. Tribol Int. 2012;55:81-86.

[34] Meng FM, Yang T. Preliminary Study on Mechanism of Cavitation in Lubricant of Textured Sliding Bearing. Proc Inst Mech Eng, Part J: J Eng Tribol. 2013;227:695-708.

[35] E W, Engquist B. The Heterogeneous Multi-Scale Methods. Comm in MathSci. 2003;1:87-133.

[36] Gao L, Hewson RW. A Multi-Scale Framework for EHL and Micro-EHL. International Tribology Conference (ITC), Hiroshima, Japan, 2011.

[37] Green n, A.E. , Rivlin RS, Shield RT. General theory of small elastic deformations superposed on large elastic deformations. Proc Roy Soc A. 1952;211:128-54.

[38] Dowson D, Higginson GR. Elasto-Hydrodynamic Lubrication, the Fundamentals of Roller and Gear Lubrication: Pergamon Press, Oxford; 1966.

[39] Barus C. Isotherms, Isopiestics and Isometrics Relative to Viscosity. Am J Sci. 1893;45:87-96.

[40] Bair S, Qureshi F. The Generalized Newtonian Fluid Model and Elastohydrodynamic Film Thickness. ASME J Tribol. 2003;125:70-75.

[41] Almqvist T, Larsson R. The Navier-Stokes Approach for Thermal EHL Line Contact Solutions. Tribol Int. 2002;35:163-70.

[42] Habchi W, Vergne P, Bair S, Andersson O, Eyheramendy D, Morales-Espejel GE. Influence of Pressure and Temperature Dependence of Thermal Properties of a Lubricant on the Behaviour of Circular TEHD Contacts. Tribol Int. 2010;43:1842-50.

[43] Dorf RC. The Engineering Handbook. US: CRC Press; 2005.

[44] Barber C, Dobkin D, Huhdanpaa H. The Quickhull algorithm for convex hulls. ACM Trans on Math Soft. 1996;22:469-83.

[45] Krupka I, Hartl M. The Effect of Surface Texturing on Thin EHD Lubrication Films. Tribol Int. 2007;40:1100-10.

Tables and Figures

Table 1 Geometrical and material parameters

Table 2 Fluid Properties

Table 3 Date selection of small scale simulations

Fig. 1 (a) Global geometry of a cylinder bearing in line contact, (b) micro pocket geometry of a unit cell on the stationary wall surface

Fig. 2 Shear-thinning and piezo-viscous fluid property

Fig. 3 Variations of the density fraction against fluid pressure described by hyperbolic tangent function

Fig. 4 Mesh sensitivity analysis on smooth surface: (a) relative errors in the large-scale pressure and mass flow rate using the solution of the finest mesh (960) as reference, (b) the large-scale pressure distributions, and (c) enlarged local pressure details of figure (b)

Fig. 5 Friction coefficient against ratio (d/L) and the minimum film thickness against cell depth (d)

Fig. 6 Newtonian solutions: (a) pressure and density fraction, (b) film thickness (textured surface with optimal parameters compared to smooth surface), (c) small scale pressure and (d) density fraction variations at different locations convergent zone $X = [0.85, 1.9]$ in the large scale geometry

Fig. 7 Piezo-viscous solutions: (a) pressure and viscosity, (b) film thickness (textured surface with optimal parameters compared to smooth surface; the arrow shows location of the minimum film thickness)

Fig. 8 Shear-thinning solutions: (a) pressure and viscosity, (b) film thickness (textured surface with optimal parameters compared to smooth surface; the arrow shows location of the minimum film thickness)

Fig. 9 Shear-thinning and piezo-viscous solutions: (a) pressure and viscosity, (b) film thickness (textured surface with optimal parameters compared to smooth surface; the arrow shows location of the minimum film thickness)

16

1
2

Table 1 Geometrical and material parameters

Cylinder radius	r = 25 mm
Micro pocket length	L= 20 μm - 200 μm
Micro pocket depth	d = 5 μm - 30 μm
Young's modulus of PTFE	E = 0.5 GPa
Poisson's ratio of PTFE	υ = 0.4
Sliding speed of smooth surface	u = 2 m/s

3
4

Table 2 Fluid Properties

5

Ambient pressure	$p_a = 10^5$ Pa
Ambient fluid density	$\rho_0 = 870$ kg/m^3
Viscosity at zero shear rate	$\eta_0 = 0.01$ Pas
Viscosity at infinite shear rate	$\eta_\infty = 0.006$ Pas
Density-pressure coefficient	$c_1 = 5.9 \times 10^8$ Pa $c_2 = 1.34$
Pressure-viscosity coefficient	$\alpha = 2.2 \times 10^{-8}$ Pa^{-1}
Critical stress at ambient pressure	$G_{cr} = 2 \times 10^4$ Pa
Power in Carreau viscosity model	$m = 0.6$
Constants in cavitation model	$k_1 = 5$ $k_2 = 1.5 \times 10^5$ Pa

6
7
8

Table 3 Date selection of small scale simulations

	Range	Number of mesh point
Gap	1- 55 μm	30
Pressure gradient	-2e10 -2e10 (N/m^3)	10
Cell inlet pressure	-0.2 – 4 (MPa)	10

9
10
11
12
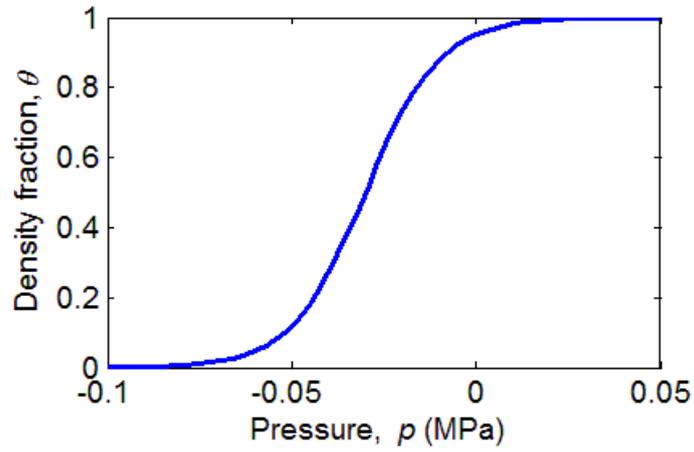
Fig. 1 (a) Global geometry of a cylinder bearing in line contact, (b) micro pocket geometry of a unit cell on the stationary wall surface (side length $|AE| = |FG| = |HB| = L/5$, $|EF| = |GH| = \sqrt{(L/5)^2 + d^2}$.)
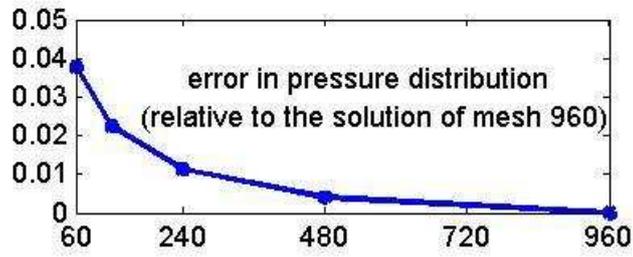
1 Fig. 2 Shear-thinning and piezo-viscous fluid property
2
3
4

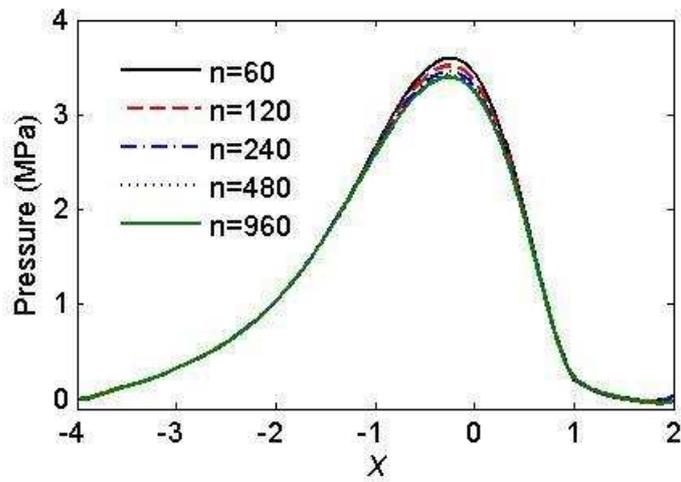5
6
7 Fig. 3 Variations of the density fraction against fluid pressure described by hyperbolic tangent
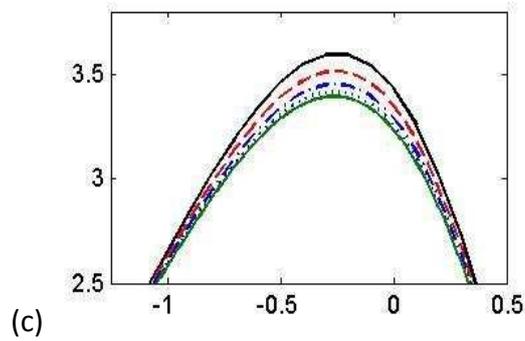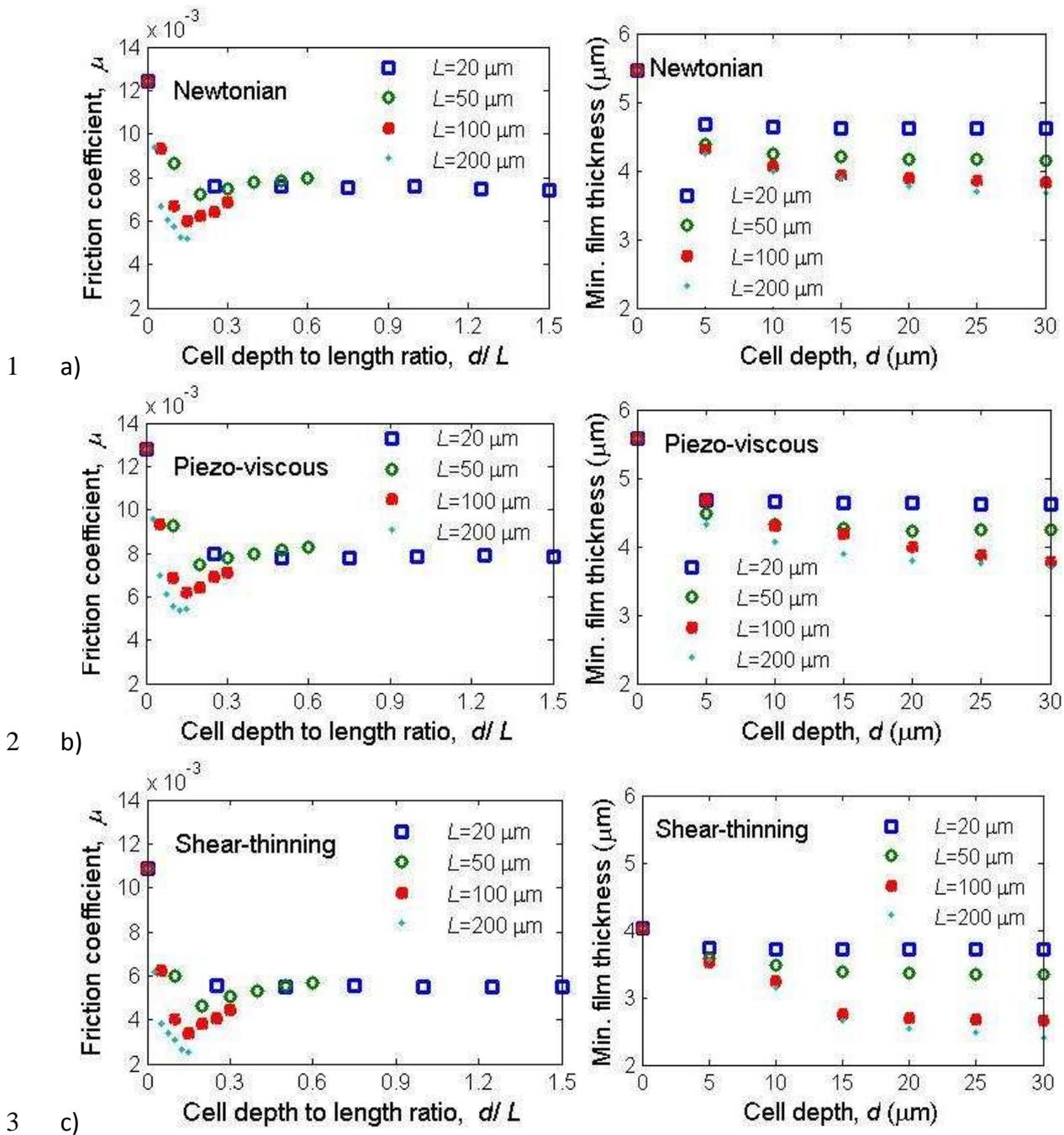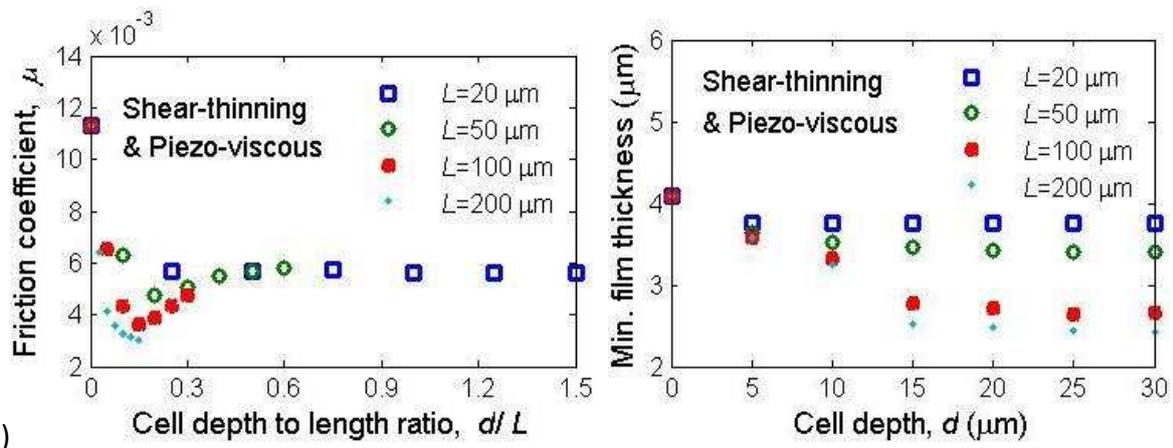8   function
9

1
2

(a)

(b)

3

4

(c)

5
6
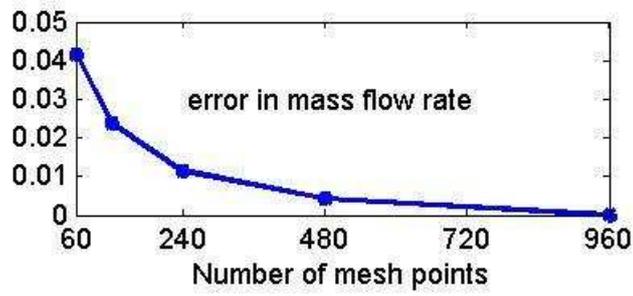
1   Fig. 4 Mesh sensitivity analysis on smooth surface: (a) relative errors in the large-scale pressure
2   and mass flow rate using the solution of the finest mesh (960) as reference, (b) the large-scale
3   pressure distributions, and (c) enlarged local pressure details of figure (b)
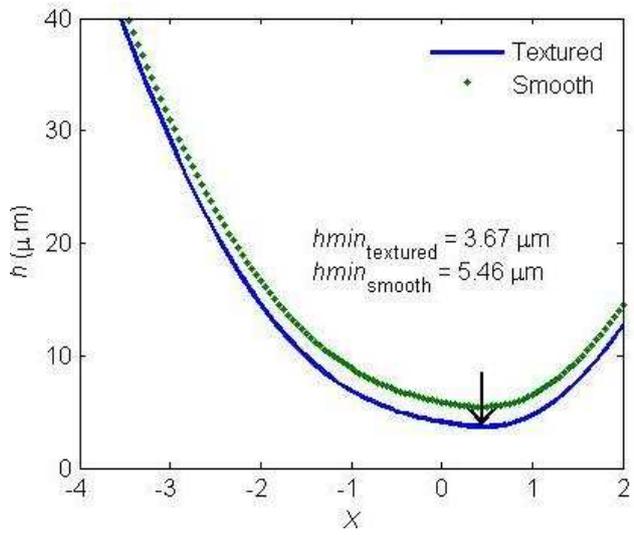4

1   a)

2   b)

3   c)

1   d)

2   Fig. 5 Friction coefficient against ratio (d/L) (left) and the minimum film thickness against cell

3   depth (d) (right); a) Newtonian; b) Peizo-viscous; c) Shear-thinning; d) Shear-thinning & Piezo-
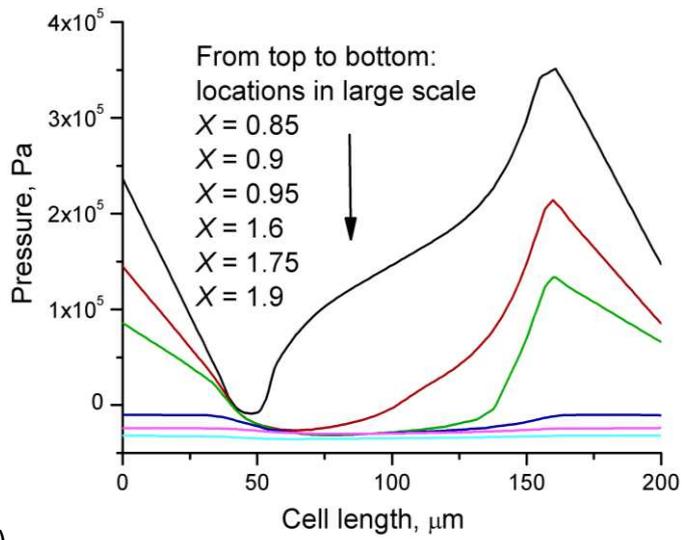
4   viscous

5
6
7
8

23

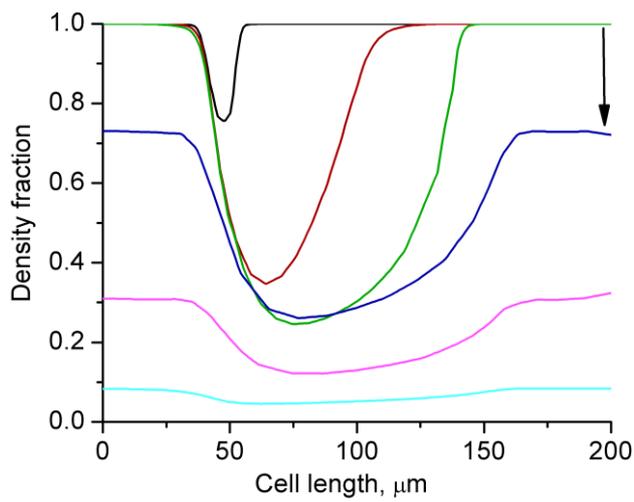1   a)   b)

2
3

From top to bottom:
locations in large scale
$X = 0.85$
$X = 0.9$
$X = 0.95$
$X = 1.6$
$X = 1.75$
$X = 1.9$
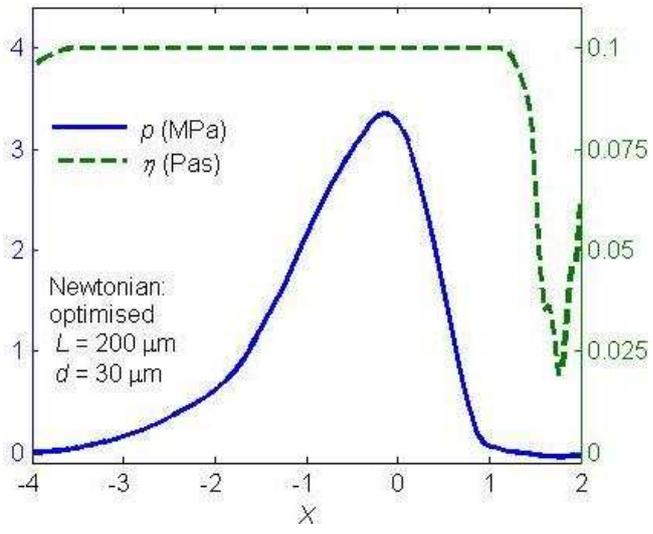
1   c)   d)
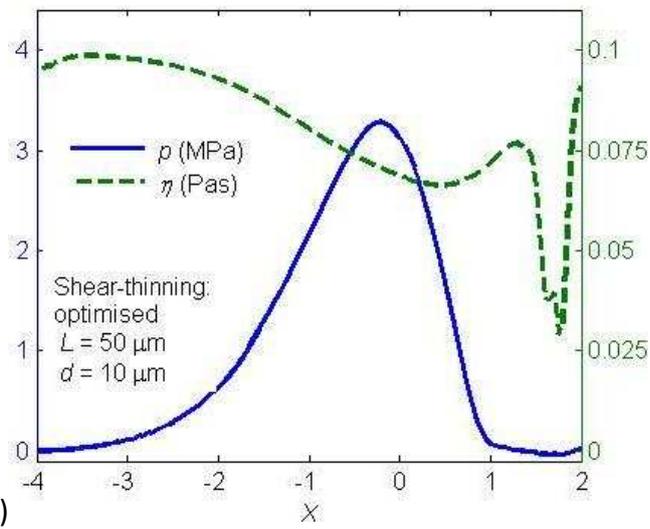

2
3
4   Fig. 6 Newtonian solutions: (a) pressure and viscosity fraction, (b) film thickness (textured
5   surface with optimal parameters compared to smooth surface), (c) small scale pressure and (d)
6   density fraction variations at different locations convergent zone $X = [0.85, 1.9]$ in the large
7   scale geometry
8

1

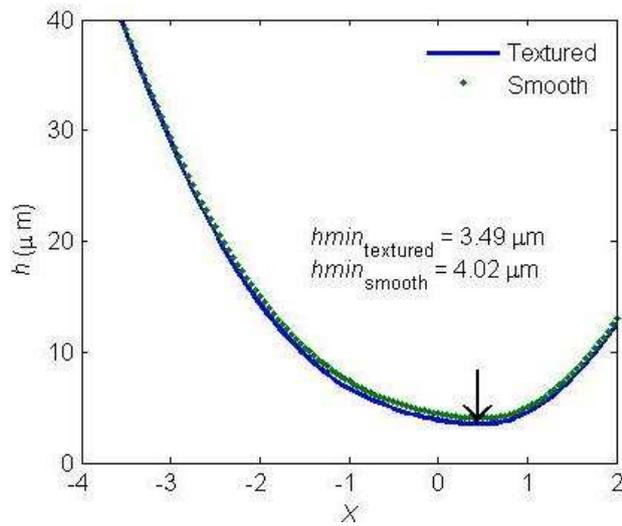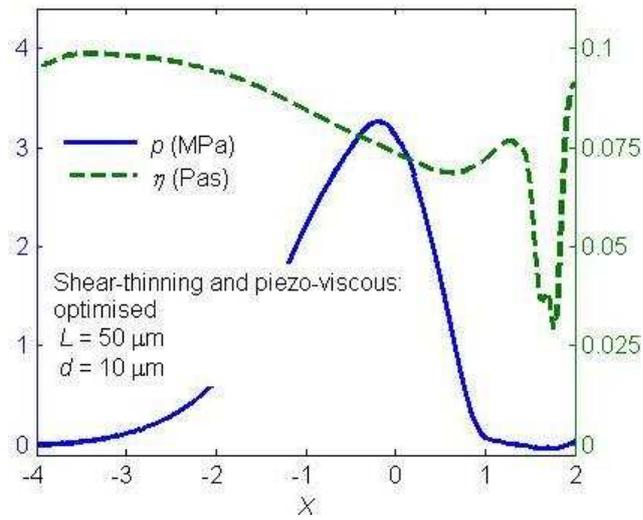2 a)   b)
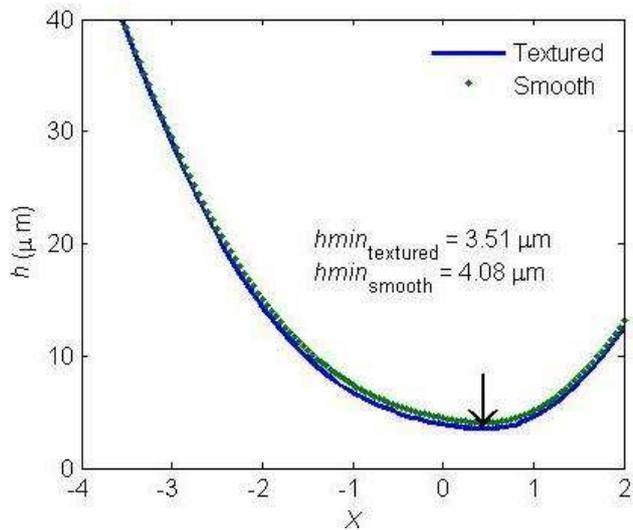

3
4 Fig. 7 Shear-thinning solutions: (a) pressure and viscosity, (b) film thickness (textured surface
5 with optimal parameters compared to smooth surface; the arrow shows location of the
6 minimum film thickness)
7

26

1   a)   b)

2
3   Fig. 8 Shear-thinning and piezo-viscous solutions: (a) pressure and viscosity, (b) film thickness
4   (textured surface with optimal parameters compared to smooth surface; the arrow shows
5   location of the minimum film thickness)
6